

# Disk-Planet Interaction Simulations: (I) Baroclinic Generation of Vortensity and Non-Axisymmetric Rossby-Wave-Instability

Shangli Ou<sup>1</sup>, Jianghui Ji<sup>2,3,4</sup>, Lin Liu<sup>5</sup>, and Xiaomeng Peng<sup>6</sup>

## ABSTRACT

We use a multi-dimensional hydrodynamics code to study the gravitational interaction between an embedded planet and a protoplanetary disk with emphasis on the generation of vortensity (potential vorticity) through a Baroclinic Instability and subsequent development of Rossby-Wave-Instability (RWI). It is found that the generation of potential vorticity is very common and effective in non-barotropic disks through the Baroclinic Instability, especially within the coorbital region. Our results also complement previous studies by Koller et al. (2003) that non-axisymmetric RWIs are likely to develop at local minima of potential vorticity distribution that are generated by the interaction between a planet and a inviscid barotropic disk. This second instability appears to be very common and robust, regardless of the equation of state, initial density distribution, and rotational law of the disk. The development of RWIs results in non-axisymmetric density blobs, which exert stronger torques onto the planet when they travel in the vicinity of the planet. As a result of that, large amplitude oscillations are introduced to the time behavior of the total torque acted on the planet by the disk. In our current simulations, RWIs do not change the overall picture of inward orbital migration but bring in a non-monotonic behavior to the migration speed. As a side effect, RWIs also introduce interesting structures into the disk. These structures may help the formation of Earth-like planets in the Habitable Zone or Hot Earths interior to a close-in giant planet.

*Subject headings:* accretion, accretion disks — Baroclinic Instability — Rossby-wave instability — hydrodynamics — numerical methods — planetary systems: protoplanetary disks

---

<sup>1</sup>High Performance Computing, Center for Computation and Technology / Information Technology Services, Louisiana State University, Baton Rouge, LA, 70803;ou@cct.lsu.edu

<sup>2</sup>Purple Mountain Observatory, Chinese Academy of Sciences, Nanjing 210008, China;jjh@pmo.ac.cn

<sup>3</sup>National Astronomical Observatory, Chinese Academy of Sciences, Beijing 100012, China

<sup>4</sup>Department of Terrestrial Magnetism, Carnegie Institute of Washington, 5241 Broad Branch Road NW, Washington, DC 20015-1305

<sup>5</sup>Department of Astronomy, Nanjing University, Nanjing 210093, China

<sup>6</sup>Department of Physics & Astronomy, Louisiana State University, Baton Rouge, LA, 70803

## 1. Introduction

Although theorists did not realize its relevance to the origin of planet when the study on the gravitational interaction between a protoplanetary disk and an embedded planet just began in late 1970s (Goldreich & Tremaine 1978), it is now one of the key ingredients of current standard theory of planet formation. According to standard core-accretion theory (Safronov 1969; Lissauer 1993), the formation of planets in circumstellar disks around T Tauri stars consists of the formation of planetesimals via collisions/coalitions of dust grains in the early stage and then gravitationally accretion after they accumulate enough mass. The life time of this T Tauri star phase is estimated to be short ( $\lesssim 10^7$  years). In order for cores of protoplanets with masses comparable to that of Jupiter to accumulate enough mass in the T Tauri stage, it is thought that their cores have to form outside the so-called “ice line”, where the distance to the central star is large (typically beyond  $\sim 4$  AU, see Ida & Lin 2004) so that the temperature is low enough to allow the condensation of gas materials to solid ice. These additional solid dusts helps to increase the dust coagulation speed and shorten the time needed to form cores of protoplanets.

Since the discovery of the first Jupiter-mass planet (Mayor & Queloz 1995) orbiting the solar-type star 51 Peg, more than 200 extrasolar planets have been discovered around the nearby stars within 200 pc (Butler et al. 2006, The Extrasolar Planets Encyclopaedia). The diversity exhibited by these planetary systems shows that the masses of these planets range from Jupiter-mass to Neptune-mass. The most prominent characteristics is that a large number of the host stars are surrounded by the so-called “hot-Jupiters” and close-in super-Earths. Around 80% of the extrasolar planets are in orbits with semi-major axes in the range  $0.01 \lesssim a \lesssim 2.5$  AU, and  $\sim 25\%$  of the total population are short-period planets<sup>1</sup> with  $a \lesssim 0.1$  AU. This has brought one of the most interesting puzzles to theorists: if protoplanets had formed in a disk region beyond  $\sim 4$  AU from the central star, how did the observed extrasolar planets end up with orbits that are so close to their host stars? If the standard theory for the formation of protoplanetary cores holds (Pollack et al. 1996; Ida & Lin 2004), then the giant planets (like hot-Jupiters) must have undergone inward orbital migration to their current locations (Lin et al. 1996).

Several mechanisms have been proposed as the drive for the migration. Some authors (Weidenschilling & Marzari 1996; Rasio & Ford 1996; Ford et al. 1999) suggested that three-body interaction between a central star and two or more planets can lead to the ejection of one of the planets, which takes away energy from the system and leaves the third object on a smaller and eccentric orbit, which is finally circularized through tidal interaction between the planet and its host star. Murray et al. (1998) suggested that resonance interactions between a planet and a disk of planetesimals can also lead to inward orbital migration of the planet. Another plausible explanation is provided by the theory of the gravitational interaction between a protoplanetary disk and an embedded planet, which was formulated, as mentioned in the beginning of this article, more than a decade before the discovery

---

<sup>1</sup>see <http://exoplanet.eu/>

of extrasolar planets.

In the third mechanism, a disk interacts with an embedded planet through their mutual gravitational forces. The planet causes the formation of spiral waves inside the disk at the Lindblad resonances; as a result of the density asymmetry induced by spiral waves, the inner disk exerts a positive gravitational torque onto the planet and the outer disk exerts a negative gravitational torque onto the planet. According to analytical analysis, the overall torque is generally negative and, hence, forces the planet to migrate inward. Ward (1997) pointed out that two major kinds of migration exist based on the mass of the embedded protoplanet. In the so called Type I migration, the planet’s mass is small and the response of the disk is linear; the migration speed is very fast so that the migration timescale is as short as  $\sim 10^4$  yr for a planetary core of  $10M_{\oplus}$  in a sufficiently viscous disk. In Type II migration, the protoplanet has enough mass to open a gap inside the disk, and migrates on a much longer viscous timescale. Besides classical analytical analysis, many groups have studied the nonlinear evolution of a disk-planet system using numerical multi-dimensional hydrodynamics (Kley 1999; Nelson et al. 2000; Papaloizou, Nelson, & Masset 2001; Nelson & Willy 2003; Bate et al. 2003, and references there in). Recently, de Val-Borro et al. (2006) also carried out a collaborative multi-code comparison research. These numerical simulations showed that the nonlinear evolution of the orbital migration of a planet inside a disk agrees with linear analysis in a qualitative manner.

However, nature is always not as simple as human beings have naively thought. Unexpected phenomena often arose in the non-linear regime. For example, Masset (2001) and Masset & Papaloizou (2003) suggested that the corotation torque originated from the coorbital region may play a very different role from that of Lindblad torques; this leads to a third kind of migration often referred to as Type III migration or runaway migration, in which the migration happens on a timescale as short as a few tens of orbits and can be directed outward in some cases. Klahr & Bodenheimer (2003) described a Baroclinic Instability in non-barotropic disks that may contribute to vorticity and global turbulences; They argued that strong vorticities may contribute to the rapid formation of Jupiter-size gas planet (Klahr & Bodenheimer 2006). Koller et al. (2003) and Li et al. (2005) showed that the so-called “Rossby-wave instabilities” may develop at the local minima of potential vorticity (PV), or vortensity (defined as the ratio between local vorticity and surface density), in an inviscid disk with initially uniform vortensity distribution.

In simulations of Li et al. (2005), these non-axisymmetric instabilities lead to the formation of vortices and density blobs, which exert stronger torque onto the planet when they travel around its vicinity and bring large oscillations to the total torque acted on the planet. They further argued that this mechanism may be possible to change the direction of the migration. Non-axisymmetric Rossby-wave instabilities are also relevant to the evolution of a single disk (Lovelace et al. 1999; Li et al. 2000) and stellar models with strong differential rotation (Ou & Tohline 2006). The time scale for RWIs to fully develop is generally on tens of dynamical time of a disk ( $\sim 100$  orbits), hence, they can not be ignored in inviscid or low viscosity cases. Therefore, it worths more labor to study their comprehensive role on planetary orbital migration and the robustness of this mechanism.

In this paper, we present results from simulations of disk-planet interaction. Our purpose is two-folded: first we wish to provide further comparisons to results presented in the collaborative comparison work of de Val-Borro et al. (2006); on the other hand, we focus more on the development of non-axisymmetric RWIs in disk models with non-barotropic equation of state (EOS) and non-uniform initial vortensity distribution, as in contrast to disk models presented in Koller et al. (2003) and Li et al. (2005), which are isothermal disks with uniform initial vortensity everywhere. In particular, we find out that the PV generation is more effective and common in disk models with non-barotropic EOS. Our results, together with those presented by Li et al. (2005), suggest that the development of RWIs is very robust in disk-planet systems with different mass distribution, rotational laws and EOSs. We also address the impact of RWIs on planet orbital migration and formation of close-in super Earths near a giant planet. In section 2, basic equations, methods and initial models are described; results from test runs are given in section 3; section 4 concentrates on the development of RWIs under certain circumstances; we close with conclusions and discussions in section 5.

## 2. Basic Equations, Methods and Initial Setup

To study the interaction between a disk and an embedded planet requires coupling hydrodynamics and orbital dynamics together. Here, we follow Nelson et al. (2000) and many previous investigations to reduce the problem to a two-dimensional (2D) one since the disk is considered to be very thin. Three dimensional (3D) investigations will be postponed to future. The fluid motion inside the disk is described by the vertically integrated continuity equation (1), radial and azimuthal components of the Navier-Stokes equation (2) and (3),

$$\frac{\partial \Sigma}{\partial t} + \nabla \cdot (\Sigma \vec{v}) = 0 \quad (1)$$

$$\frac{\partial(\Sigma v_r)}{\partial t} + \nabla \cdot (\Sigma v_r \vec{v}) = \frac{\Sigma v_\phi^2}{r} - \frac{\partial P}{\partial r} - \Sigma \frac{\partial \Phi}{\partial r} + f_r \quad (2)$$

$$\frac{\partial(\Sigma v_\phi)}{\partial t} + \nabla \cdot (\Sigma v_\phi \vec{v}) = -\frac{\Sigma v_r v_\phi}{r} - \frac{1}{r} \frac{\partial P}{\partial \phi} - \frac{\Sigma}{r} \frac{\partial \Phi}{\partial \phi} + f_\phi, \quad (3)$$

where  $\Sigma$  is disk surface density,  $\vec{v}$  is two fluid velocities,  $P$  is vertically integrated pressure,  $f_r$  and  $f_\phi$  are two components of viscous forces, and  $\Phi$  is the gravitational potential felt by fluid elements. Details regarding viscous terms can be found in Nelson et al. (2000). The EOS of the disk fluid is considered as locally isothermal (Nelson et al. 2000) as given in below

$$P = c_s^2 \Sigma, \quad (4)$$

where the local isothermal sound speed is  $c_s = \frac{H}{r} \sqrt{GM_*/r}$  with disk aspect ratio  $H/r = 0.05$ . (As will be discussed in details later, this radial variation of sound speed generates vorticity wherever an azimuthal density gradient exists.)

We further simplify our study to non-self-gravitational systems, in which the self-gravity of the fluid is not taken into account for the fluid motion; hence,  $\Phi = \Phi_* + \Phi_p$ , where  $\Phi_*$  is the potential field of the central star and  $\Phi_p$  is the potential field of the planet, which is given by  $\Phi_p = -M_p/\sqrt{r^2 + \epsilon^2}$ , where  $M_p$  is the planet mass and  $\epsilon$  is taken to be 0.2 of the Roche Lobe of the planet. The initial disk model has Keplerian rotational profile and uniform density, which results in an initial radial vortensity profile  $\xi(r)$  that is proportional to  $r^{-\frac{3}{2}}$  (vortensity is defined as the ratio between local vorticity and surface density). The value of density and viscosity are chosen to follow those specified in de Val-Borro et al. (2006). The disk and the non-rotating coordinate system are centered at the central star instead of the center of mass of the system, which locates slightly off the central star. To handle the hydrodynamics part, we adopted a legacy code developed by the astrophysical group at Louisiana State University to study star formation (Tohline 1980; Williams & Tohline 1988), mass transferring binary stars (Motl, Tohline, & Frank 2002), and rotating instabilities in neutron stars (Ou & Tohline 2006). The code is explicit and 2nd order in both space and time. It splits the source term and advection term in a manner similar to Zeus (Stone & Norman 1992). Other features implemented include Van Leer upwind scheme, artificial viscosity to handle shock, and, staggered cylindrical grids. The code is originally three-dimensional, but adapted to 2D in this work. At the boundary of our computational grids, mass is allowed to flow off the grids but no inflow is allowed. We also implemented the wave-killing boundary condition specified in de Val-Borro et al. (2006) for comparison purpose.

The equation of motion for the planet is:

$$\frac{d^2 \vec{r}_p}{dt^2} = -\frac{G(M_* + M_p)}{r_p^3} \vec{r}_p - G \int \frac{\Sigma(\vec{r}')}{(|\vec{r}_p - \vec{r}'|^2 + \epsilon^2)^{\frac{3}{2}}} (\vec{r}_p - \vec{r}') r' dr' d\phi \quad (5)$$

where the first term on the right is derived from the relative motion of the planet to the central star, the second term is the gravitational force exerted on the planet by the disk. For comparisons with previous investigations (Li et al. 2005; de Val-Borro et al. 2006), we turned off the disk’s attraction in many of our simulations so that the planet stays on a fixed circular orbit at 1 AU; for certain runs, the disk potential was turned on to allow the planet to move so that we can assess RWI’s role on the migration. A 4th order Runge-Kutta integrator is used to integrate forward the equation of motion of the planet during each Courant timestep as required by the hydro part. To compute the torque acted on the planet, we followed the specification in de Val-Borro et al. (2006),

$$T_z = GM_p \int \Sigma \vec{r}_p \times \frac{(\vec{r}' - \vec{r}_p)}{(|\vec{r}' - \vec{r}_p|^2 + \epsilon^2)^{\frac{3}{2}}} r' dr' d\phi, \quad (6)$$

torques from inside and outside the Roche-lobe of the planet are computed separately for both inner disk and outer disk. In the following sections, we show time evolution of the total torque including contributions from within and outside the Roche-lobe, the temporal behavior of the total torque does not change qualitatively when torques from within the Roche-lobe are excluded.

In equations of motion for both the planet and disk, we neglected the indirect terms due to the acceleration to our coordinate system by the disk (the planet’s acceleration to the coordinate

system is neglected for the disk evolution as well). Since the difference between the center of the mass and our coordinate origin is fairly small, we expect the effect of indirect terms won't be significant to change our results qualitatively; hence we dropped these terms from our equations to save computing time. (The evaluation of these indirect terms involves integrals over the mass distribution and is therefore relatively expensive.) Finally, the accretion onto the planet is neglected as well.

The units adopted are the following: the gravitational constant  $G = 1$ , length unit is 1  $AU$ , and  $M_* + M_p = 1$ . These setups help us to have a direct comparison between our results and those presented in de Val-Borro et al. (2006). A Jupiter mass is defined as  $10^{-3}$  and a Neptune mass is defined as  $10^{-4}$ . The planet's mass is turned on gradually in the first 5 orbits. As shown in Li et al. (2005), very high resolution is required to resolve RWIs. This limits our ability to push simulations to much longer time scale. In general, we only advance our simulations to  $\sim 200$  orbits, which is sufficient for RWIs to fully develop.

### 3. Test Runs for Jupiter mass planet

In this section, we present results for interaction between a disk and a Jupiter mass planet on a fixed orbit as a calibration to our code. According to previous analytical analysis and numerical nonlinear studies (Lin & Papaloizou 1986; Trilling et al. 1998; Nelson et al. 2000), a Jupiter mass planet is capable of clearing most of the materials around its orbit and opening a fairly wide and deep gap in a viscous/inviscid disk. In order to test whether our code can simulate this correctly, we have run this configuration for both viscous and inviscid disks on grids with two different resolutions,  $128 \times 384$  and  $256 \times 512$ , to check for convergence. To avoid lengthy descriptions, we only show results for a viscous disk.

Figure 1 displays radial profiles of surface density  $\Sigma$  and vortensity  $\xi$  averaged over the azimuthal direction at  $t \approx 0, 100, 200$  orbits for the higher resolution run. At the final age, a wide and deep gap has been opened from the initial flat density profile, the contrast between the lowest and highest density spans over around two orders of magnitude. Inside the gap where the surface density is extremely low, the vortensity has increased to a very high level. (Notice that the vortensity is normalized to its initial value at  $r = 1$ .) Two vortensity minima formed around the inner and outer edge of the gap, where RWIs are expected to grow. But since surface density inside the gap is extremely low, we don't expect it to have significant effect on the evolution. (We note that the existence of viscosity also affects the development of RWIs.) To compare with plots presented in de Val-Borro et al. (2006), a logarithmic color map of surface density distribution of the disk at  $t \approx 200$  orbits is shown in Figure 2. It is observed that spiral arms originating from the planet forms in both the inner and outer disks. These two spiral arms are well-known Lindblad waves caused by the potential of the planet and, in turn, exert a negative total torque onto the planet as predicted by classical theory (Goldreich & Tremaine 1978; Lin & Papaloizou 1980). The structures shown in this plot agree qualitatively with those shown in de Val-Borro et al. (2006, see their Fig.

10).

Figure 3 illustrates the evolution of the total torque (per unit mass) exerted on the planet by the disk for both lower and higher resolution runs. The data have been smoothed using a moving box method over 10 orbit period (Nelson et al. 2000). Their behaviors agree closely with each other, which suggests that we have achieved convergence on these results. As expected, the total torque has a slightly negative value and will drive the planet to migrate inward gradually. The magnitude of the torque falls in the same range of those presented in a recent collaborative comparison study (de Val-Borro et al. 2006, see their Table 6). We also monitored the mass in the computational grids, there are around 93% of the initial mass left at the end of the higher resolution run.

In general, our test runs for Jupiter mass planet agree with previous investigations in a qualitative manner. In the following, we will switch to the situation of a Neptune-mass planet embedded in a protoplanetary disk and study the development of RWIs in such configurations.

#### 4. High Resolution runs for RWI in protoplanetary disk with a Neptune-mass planet

##### 4.1. Results for simulations with a Neptune mass planet on a fixed orbit

In this subsection, we present results from a series of simulations in which a Neptune-mass planet is on a fixed circular orbit. Previous investigations (Nelson et al. 2000; de Val-Borro et al. 2006) have shown that a Neptune-mass planet can only creates a shallower and narrower gap inside a disk due to its smaller mass. Koller et al. (2003) and Li et al. (2005) further suggested that, in an inviscid disk with a Neptunian mass planet, radial vortensity minima are important because they may trigger RWIs to develop. As a result of RWI, non-axisymmetric density blobs form and orbit around the central star; the torque exerted on the planet by the disk can undergo large amplitude oscillations as these density blobs pass by the vicinity of the planet and apply gravitational perturbations to it. As suggested by Li et al. (2005), this mechanism may potentially slow down the inward migration of a planet and, in some extremely cases, even change the sign of the total torque exerted on the planet and, thus, cause it to migrate outward.

Since the disk models studied in Koller et al. (2003) and Li et al. (2005) have an isothermal EOS and an initial flat vortensity profile, we wish to investigate if the same mechanism will also work in disks with non-barotropic EOS and non-uniform vortensity. With this in mind, we adopted Keplerian disk models similar to those of de Val-Borro et al. (2006), which has a locally isothermal EOS and an initial uniform surface density and, hence, an initial monotonically decreasing vortensity profile as proceeding outward radially. We carried out simulations of this configuration on grids with resolutions of  $128 \times 384$ ,  $400 \times 800$ , and  $400 \times 1600$ ; a simulation with a resolution of  $800 \times 3200$  was also performed for  $\sim 70$  orbits to check for the convergence of vortensity profile. The viscosity is turned off in these simulations.

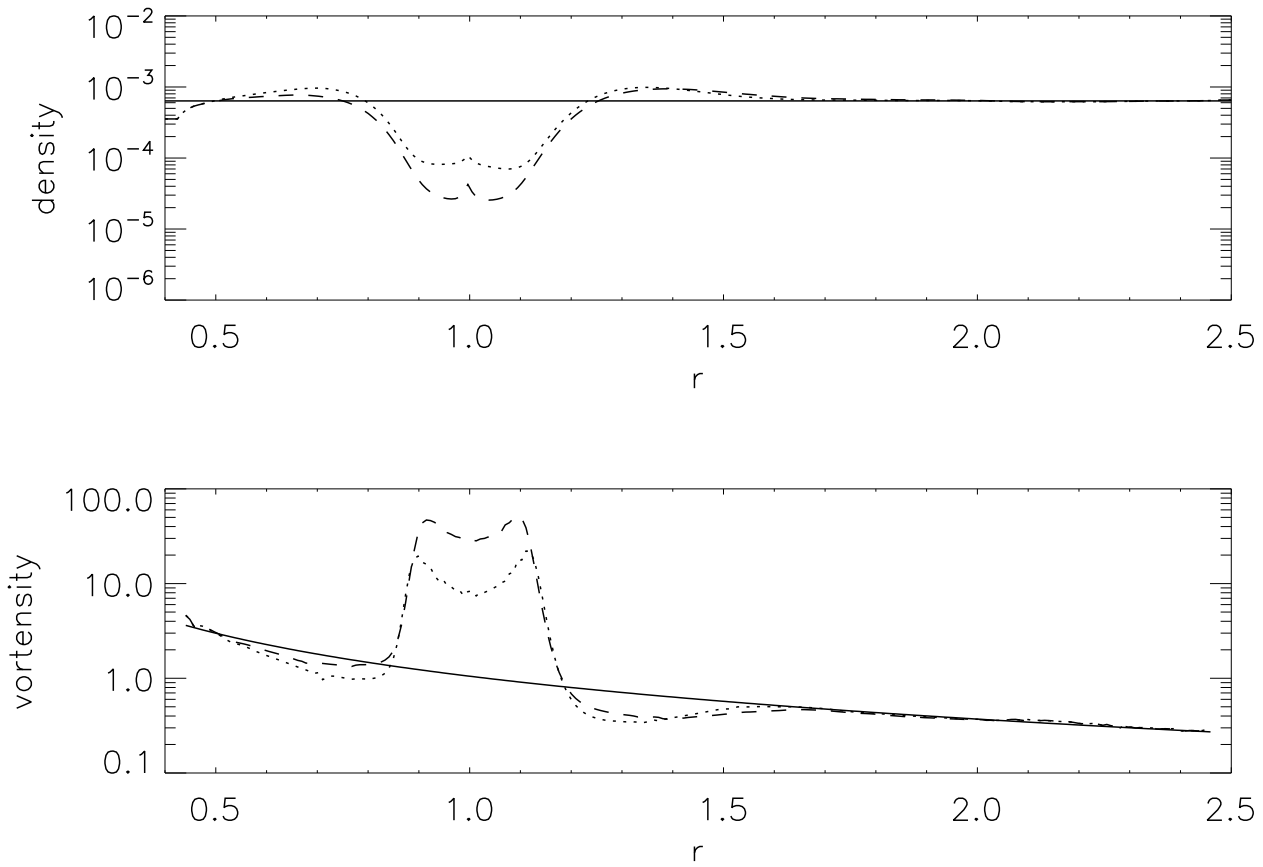


Fig. 1.— The top and bottom panels show, respectively,  $\Sigma(R)$  and  $\xi(R)$  of a viscous disk with a Jupiter mass planet averaged azimuthally at  $t \approx 0$  (solid line), 100 (dotted line), and 200 (dashed line) orbits for the higher resolution run ( $256 \times 512$ ).



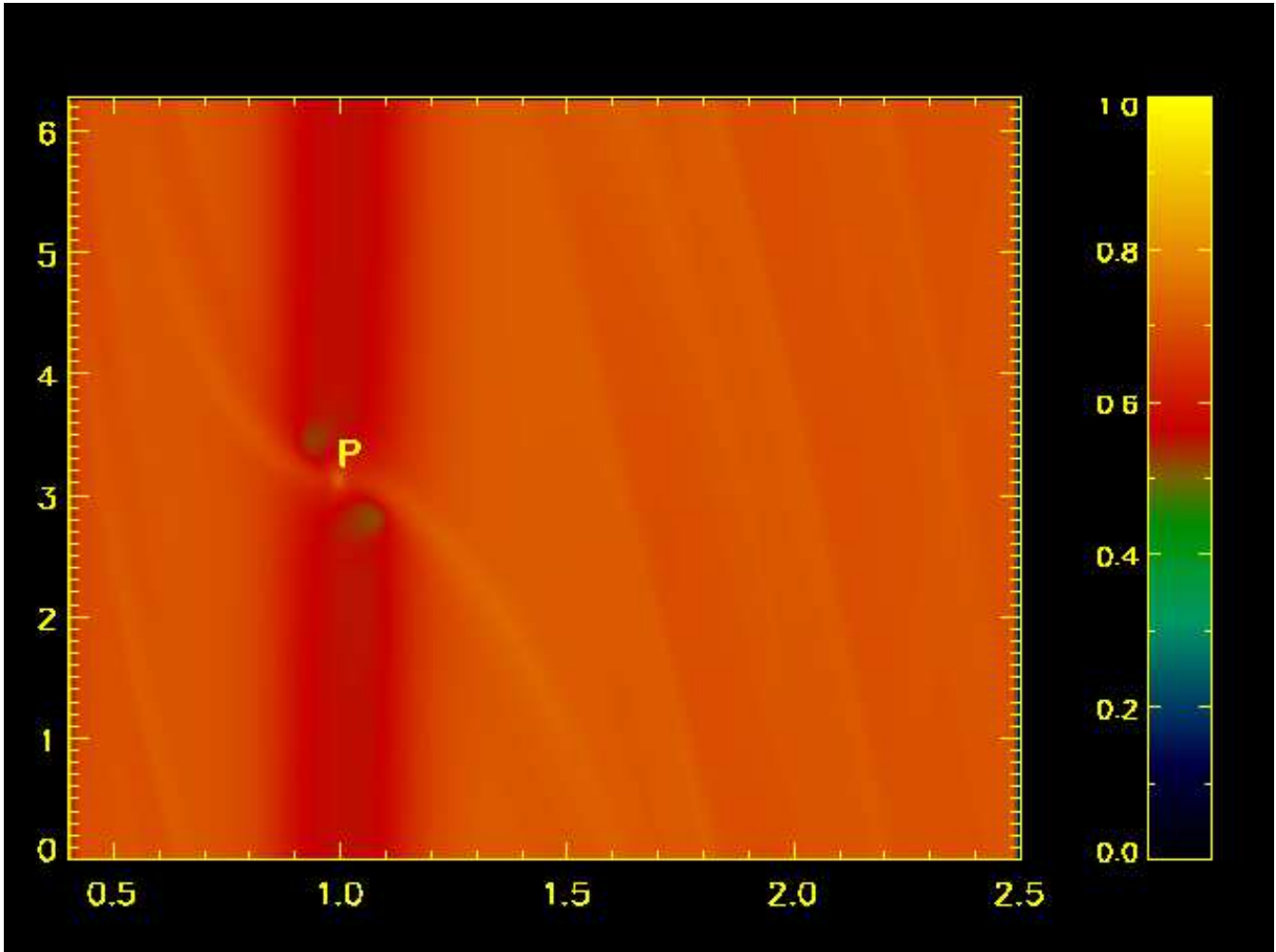


Fig. 2.— Logarithmic color map of surface density distribution for a viscous disk with a Jupiter mass planet at  $t \approx 200$  orbits for the higher resolution run ( $256 \times 512$ ). The horizontal axis is the radial axis ranging from 0.4 to 2.5, and the vertical axis is the azimuthal direction spanning over  $2\pi$  range with the planet shifted to around the middle. A letter “P” is labeled next to the location of the planet. The color bar represents relative rather than absolute values.

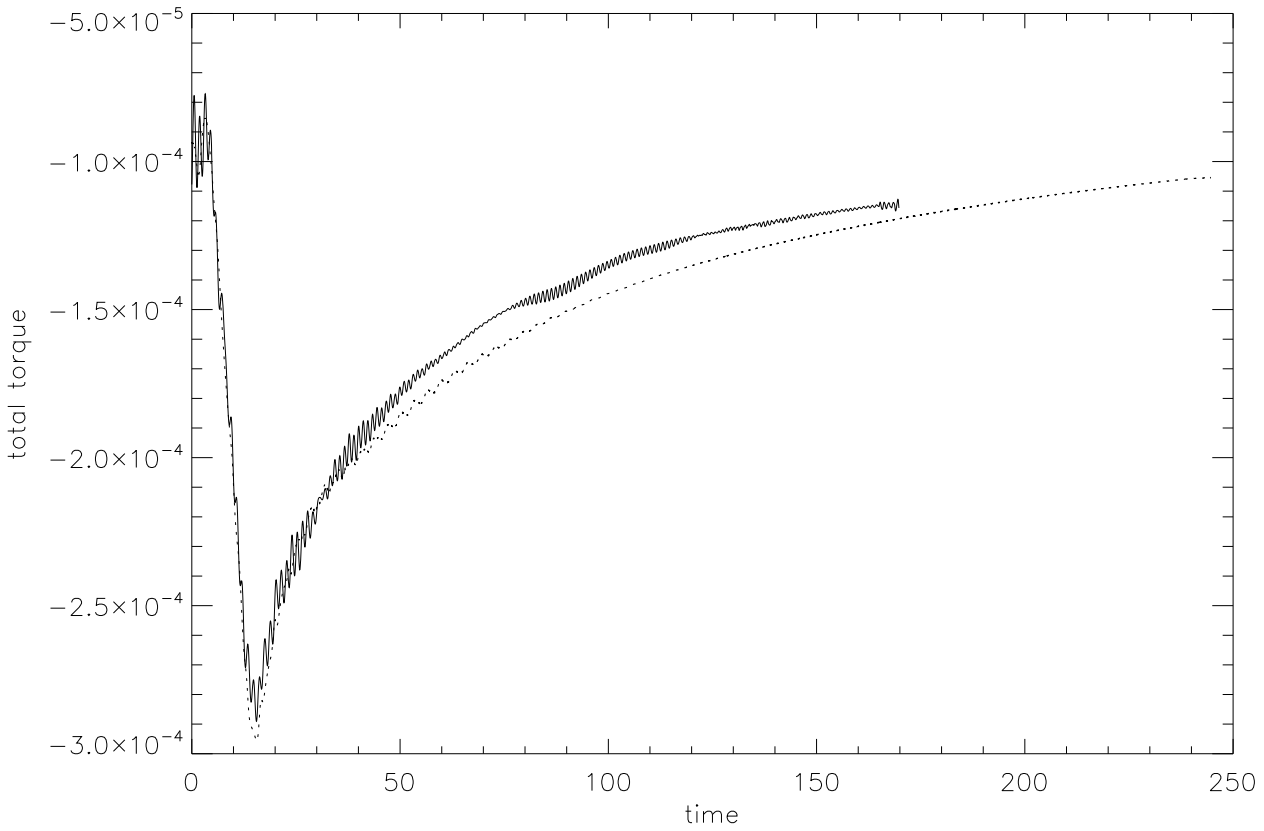


Fig. 3.— Time evolutions of the total torque (per unit mass) exerted on a Jupiter mass planet by the disk for lower (solid line) and higher (dotted line) resolutions

In general, our simulations show that the evolution of the system consists of two stages: the first stage is the formation of two spiral arms which exert a negative torque to the planet; the second stage is the development of RWIs in valleys (minima) of the radial vortensity profile some time after the formation of spiral arms. However, fine structures are only resolved accurately in higher resolution runs, mainly because interactions happen mostly around the co-orbital region (Li et al. 2005). In the following, we show detailed results from a run with a resolution of  $400 \times 1600$ .

Figure 4 displays radial profiles of  $\Sigma$  and  $\xi$  averaged over the azimuthal direction at  $t \approx 0, 60, 120$  orbits. In order to give a better view of fine structures around the co-orbital region, only regions from  $r = 0.6$  to  $r = 1.4$  are shown in the plot. Compared to the case of a Jupiter mass planet, a Neptune mass planet only opens a relatively shallower and narrower density gap. The contrast between the lowest and highest density is around a factor of two. Since the surface density inside the gap is not quite low, the vortensity there does not increase to much high level. (Notice that the vortensity is normalized to its initial value at  $r = 1$ .) However, three vortensity valleys formed across this radial region, with one centered around the planet’s orbit. Because the density inside the gap is still significant, RWIs resulted from these vortensity minima will have important effect on the evolution of the system (Li et al. 2005).

A linear color map of surface density distribution on a polar plot (Li et al. 2005) at  $t \approx 150$  orbits is illustrated in Figure 5. Focusing on the formation of high density areas (red/brown regions), we observe not only red Lindblad spiral arms, but also, other non-axisymmetric high density structures at different locations: the inner edge of the outer disk (brown arc-shaped region centered around 7 o'clock), the outer edge of the inner disk (red/brown arc-shaped region around its edge); interestingly, the density inside the gap is no longer axisymmetric any more, as suggested by the light blue region around 10 o'clock. The radial locations of these non-axisymmetric structures match exactly with the local minima of the vortensity distribution (see bottom portion of Figure 4) as predicted by linear analysis (Li et al. 2000).

Figure 6 shows the time evolution of the total torque on the planet, the torque from the inner and outer disk. The behavior of the total torque is totally different from that in the Jupiter mass case: very large amplitude oscillations present through most of the simulation. As pointed out by Li et al. (2005), these oscillations are caused by the gravitational pull from those orbiting density blobs; each time when they pass the vicinity of the planet, they exert a stronger torque onto the planet, the sign of their torques depends on their relative position to the planet. The existence of these oscillations complicates the classical picture of the gravitational torque exerted on the planet by the disk.

Figure 7 exhibits the radial profile of the specific angular momentum  $J$  inside the disk around the co-orbital region at different time. The solid line denotes for initial Keplerian profile, dotted, dashed, and dotted-dashed lines denote for profiles at later times. As the evolution goes on, the inner disk exerts a positive torque to the planet and, hence, is giving away angular momentum to the planet; whereas, the outer disk exerts a negative angular momentum to the disk, thus, is

gaining angular momentum from the planet; therefore, the angular momentum is being transferred from the inner disk to the outer disk due to the interaction between the planet and the disk. This mechanism results in a dip in the inner disk’s  $J$  profile but a bump in the outer disk’s  $J$  profile. As a result, an S-shaped structure formed in the vicinity of the planet’s fixed orbit. Again, for comparison to previous studies, there are around 98% masses left in the grid at the end of the highest resolution run.

In summary, our results of the development of RWIs in an inviscid disk with a Neptune-mass planet on a fixed orbit are in agreement with those of Li et al. (2005); however, they differ in some key physical quantities. In particular, the PV maxima in Li et al. (2005, see their Figure 2 and 9) are located at radii outside the coorbital region where shocks present; whereas, PV maxima in our simulations reside within the coorbital region around  $0.95 < r < 1.05$ , where shocks are not expected to occur. This discrepancy raises some concerns. Because based on the evolution equation of vorticity  $\vec{\zeta}$ :

$$\frac{d\vec{\zeta}}{dt} = \frac{\nabla\Sigma \times \nabla P}{\Sigma^2} \quad (7)$$

the vorticity can only be generated at regions where pressure gradient and density gradient do not align with each other; such generation of vorticity normally happens around shocks in barotropic disks as illustrated in Li et al. (2005), which contributes to vortensity maxima outside the coorbital region.

To understand the mechanism that generates vortensity (PV) maxima within the coorbital region in our simulations, we note that our disk models have a non-barotropic EOS with a radial variation of sound speed  $c_s$ , which also brings in misalignment of pressure gradient and density gradient wherever azimuthal density gradient appears ( $\nabla c_s \times \nabla\Sigma \neq 0$ ). This misalignment acts as a source term for the generation of vorticity within the coorbital region, where no shock but strong azimuthal density gradient presents. Therefore, the large density depression in the same region naturally gives birth to vortensity increment. According to Li et al. (2005), lower resolution may result in unphysical generation of vortensity. To further test that if our results are resolution-dependent, we carried out a run with resolution  $800 \times 3200$  for  $\sim 70$  orbits (due to the limitation of computational resources). Figure 8 shows the vortensity profile around coorbital regions for runs with different resolutions at  $t \approx 70$  orbits. They all exhibit vortensity maxima within the coorbital region, which indicates that our results are resolution-independent. As a further evidence that vortensity is generated around where azimuthal density gradient exists, Figure 9 and 10 illustrate the distribution of vortensity increment and azimuthal density gradient, respectively, for the run with resolution  $800 \times 3200$  at  $t \sim 70$  orbits. For a better view, they are zoomed in the neighborhood of the planet. It is observed that vortensity is generated within the Roche lobe, where strong azimuthal density gradient, instead of shocks, exists. Such a generating mechanism of vortensity inside a planet’s Roche lobe has the same origin as baroclinic instability discussed in Klahr & Bodenheimer (2003), which contributes to global turbulence within the disk. On the other hand, we also note that the oscillations of the torque acted on a neptune mass planet appear much earlier in our simulations ( $\sim 50$  orbits in our Figure 6) than they do in Li et al. (2005,  $\sim 200$

orbits in their Figure 6), which suggests that PV (vortensity) generation is even more effective and common in non-barotropic disk models.

As show in Figure 10, the azimuthal density gradient flips the sign across the planet; thus, we expect the vortensity increment also flip the sign there. However, the vortensity change within the Roche-lobe shown in Figure 9 is always positive. We don't fully understand the underlying physics of this phenomenon, but suspect that this is possibly due to vortensity mixture along librating stream lines in the horse region, i.e., where fluid elements make the U-turn. A detailed and vigorous analysis of fluid motion and vortensity mixture around a Neptune-mass planet embedded in a non-barotropic disk is beyond the scope of this paper, and will be studied in a separate investigation.

Since the generation of vortensity in non-barotropic disks turns out to be quite universal, the second instability (RWIs) triggered around vortensity extrema is probably more common in realistic situations than what has been thought previously; it will have strong influence on the migration of a neptune mass planet in an inviscid disk. Next, we will discuss the case in which the planet is allowed to move freely under the torque action from the disk.

#### 4.2. Simulation for a freely moving Neptune-mass planet

In order to assess possible roles of RWIs on the migration of a planet, we carried out two simulations in which a Neptune mass planet is allowed to move under the influence of the gravitational torque from the disk. The resolutions are  $400 \times 800$  and  $400 \times 1600$ . In these two simulations, the planet is fixed on the initial circular orbit for the first 50 orbits (slightly longer than the libration period for the neptune mass planet) to allow the disk to respond properly, it is then released to move freely under the influence of the torque from the disk. The results from these two simulations are similar to each other, which suggests that convergence is achieved. We use the higher resolution run to present the evolution of the system.

Figure 11 illustrates radial profiles of  $\Sigma$  and  $\xi$  averaged over the azimuthal direction at  $t \approx 50, 100, 150, 200$  orbits. It is observed that at  $t = 50$  orbits the planet has created a shallow gap within the disk around  $r = 1$ , the density level is enhanced at both the inner and outer edge of the gap ( $r \approx 0.88$  and  $r \approx 1.12$ ). Then, the planet migrates inward when  $t > 50$  orbits as an effect of an overall negative total torque. As it moves in, the surface density gap and vortensity valleys also migrate with it. On the other hand, a shallower density gap and a vortensity valley are still preserved around its initial orbital location.

Figure 12 exhibits the time evolution of the total torque acted on the planet and its radius to the central star. The overall torque exerted on the planet is negative in average throughout the simulation, but undergoes some changes. After the whole system settles down in the first 50 orbits, large amplitude oscillations with certain period show up; the torque becomes increasingly negative when the planet starts to migrate inward; it then reaches its peak in magnitude at  $t \approx 100$  orbits ( $\sim 50$  orbits after releasing); after that, it is weakened and then returns back to a very small

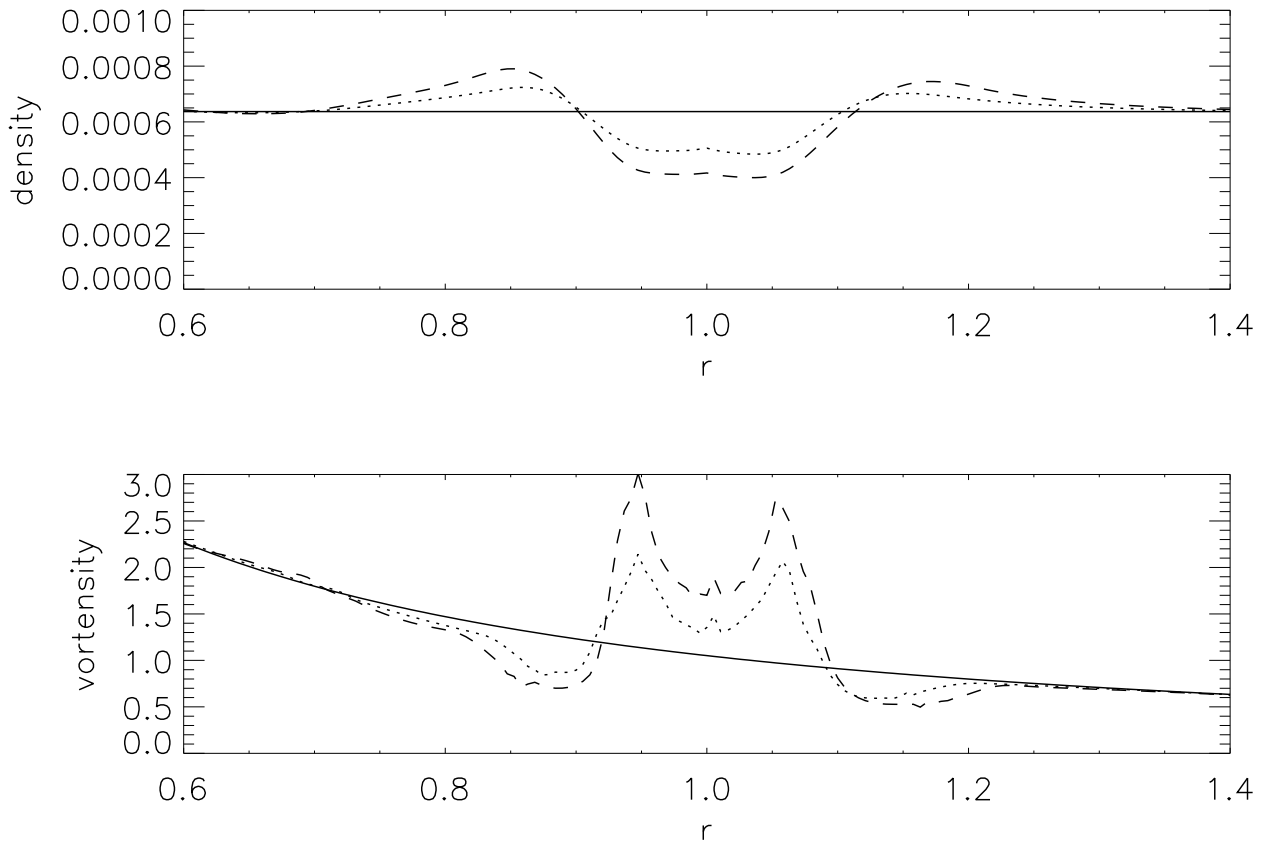


Fig. 4.— The top and bottom panels show, respectively,  $\Sigma(R)$  and  $\xi(R)$  of the disk with a Neptune mass planet averaged azimuthally at  $t \approx 0$  (solid line), 60 (dotted line), and 120 (dashed line) orbits.

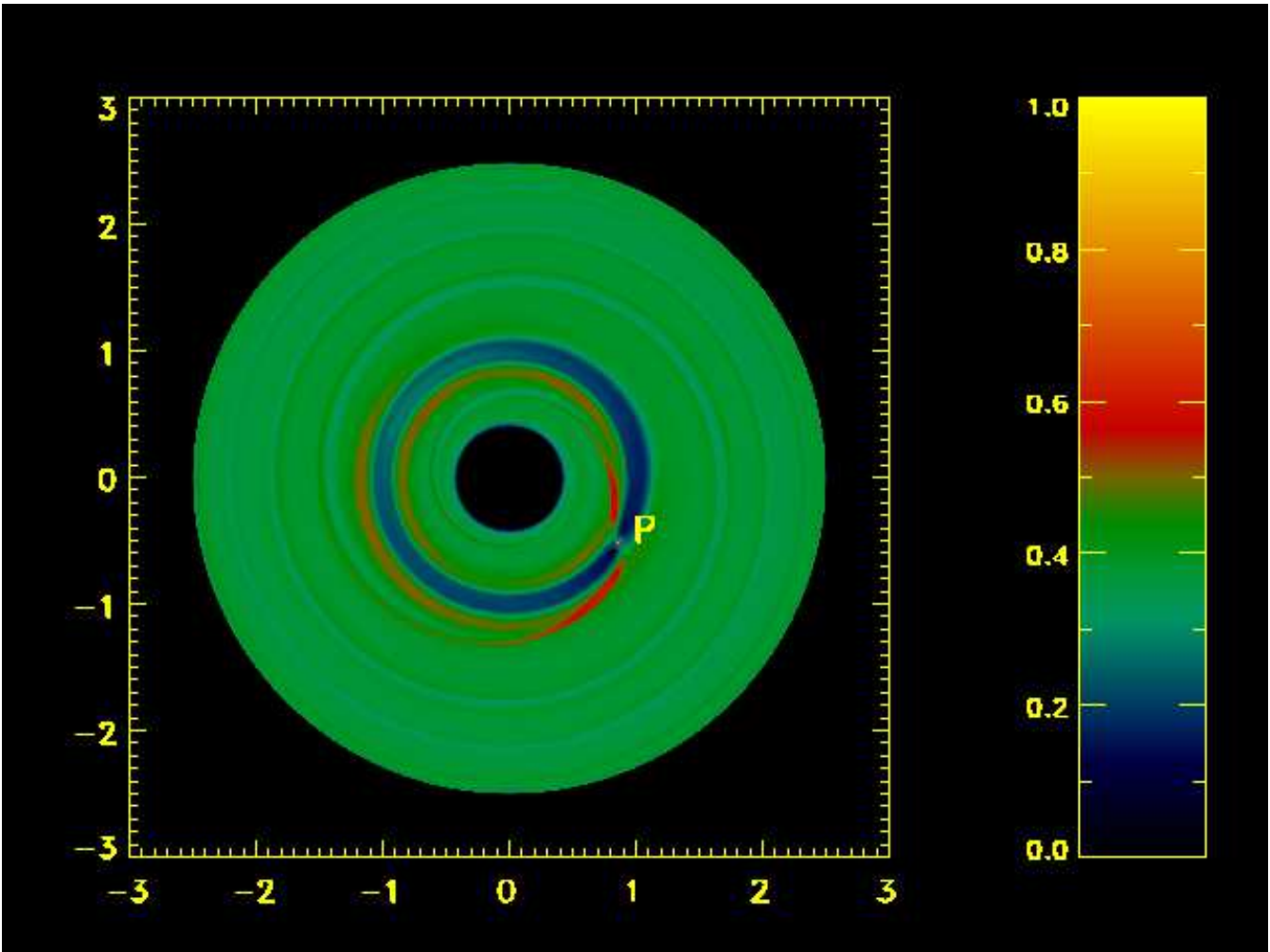


Fig. 5.— The same as Fig. 2 but in linear scale for an inviscid disk with a Neptune mass planet at  $t \approx 150$  orbits. A letter “P” is labeled next to the location of the planet. The color bar represents relative rather than absolute values.

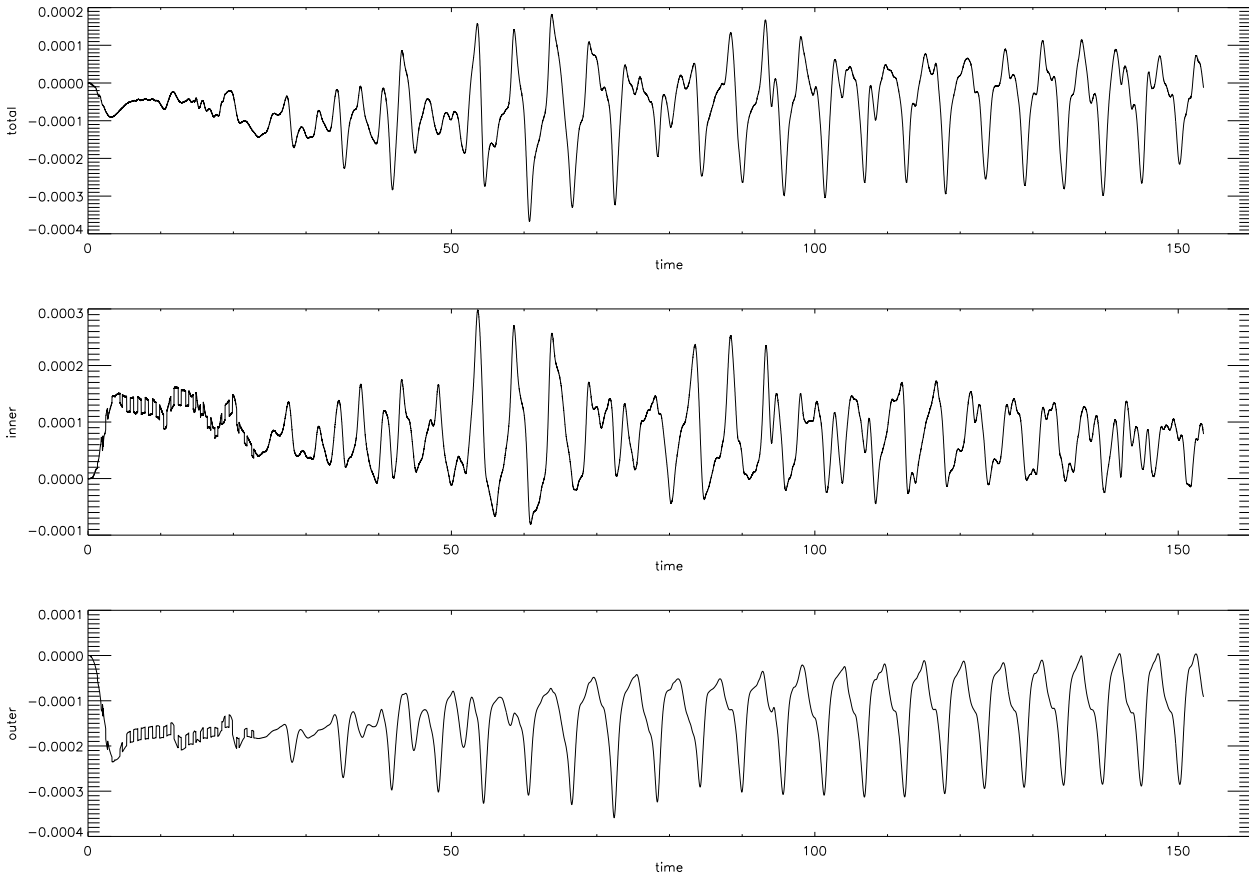


Fig. 6.— Time evolutions of total torque (top), torques from the inner (middle) and outer (bottom) disks exerted on a Neptune mass planet for the highest resolution run ( $400 \times 1600$ ). Raw data is shown.



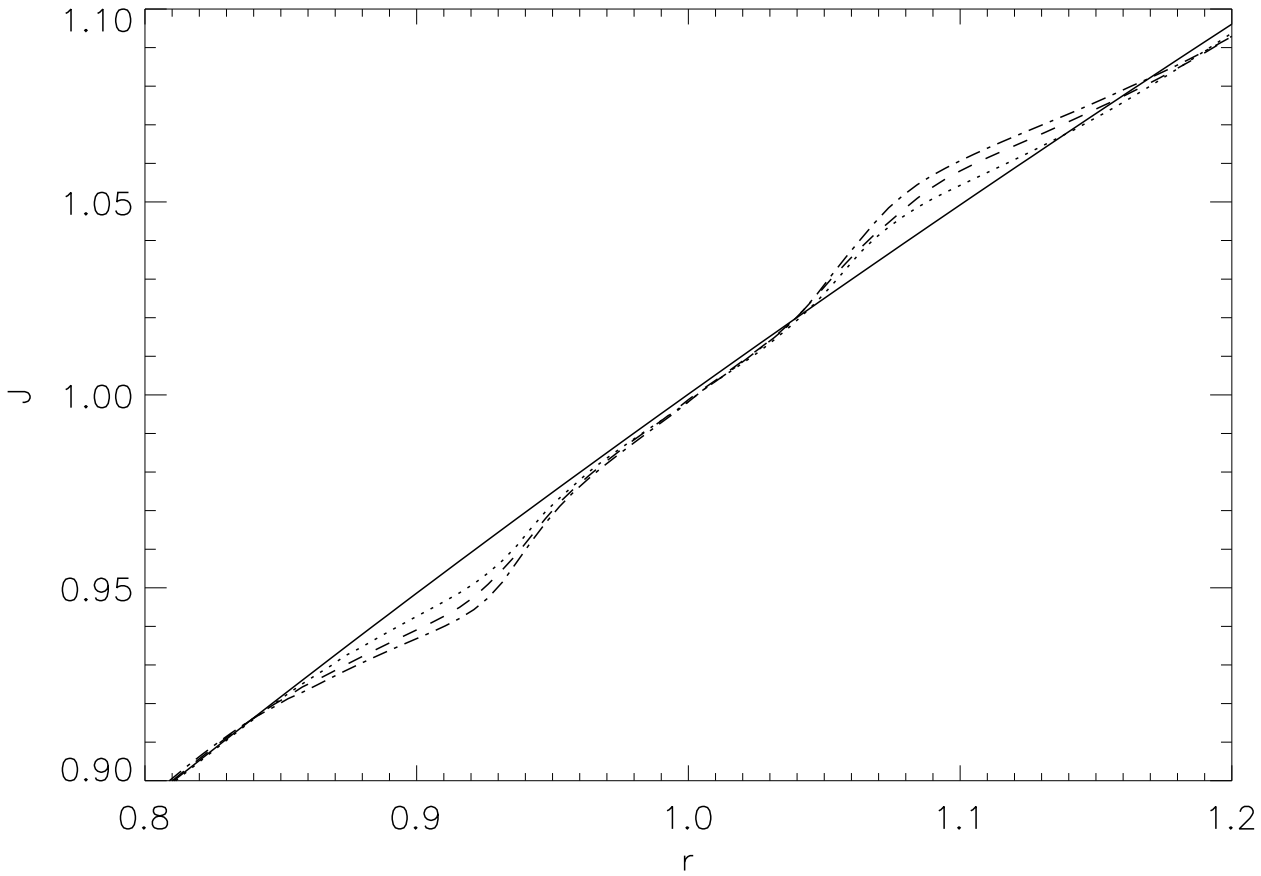


Fig. 7.— Radial profiles of specific angular momentum around the co-orbital region of the disk with a Neptune mass planet at different times. The solid line denotes for initial Keplerian profile, dotted, dashed, and dotted-dashed lines denote for profiles at later times. Data have been normalized to the initial value at  $r = 1$ . As evolutions goes on, angular momentum is being removed in the inner region but added to the exterior region due to the interaction between the disk and the planet.

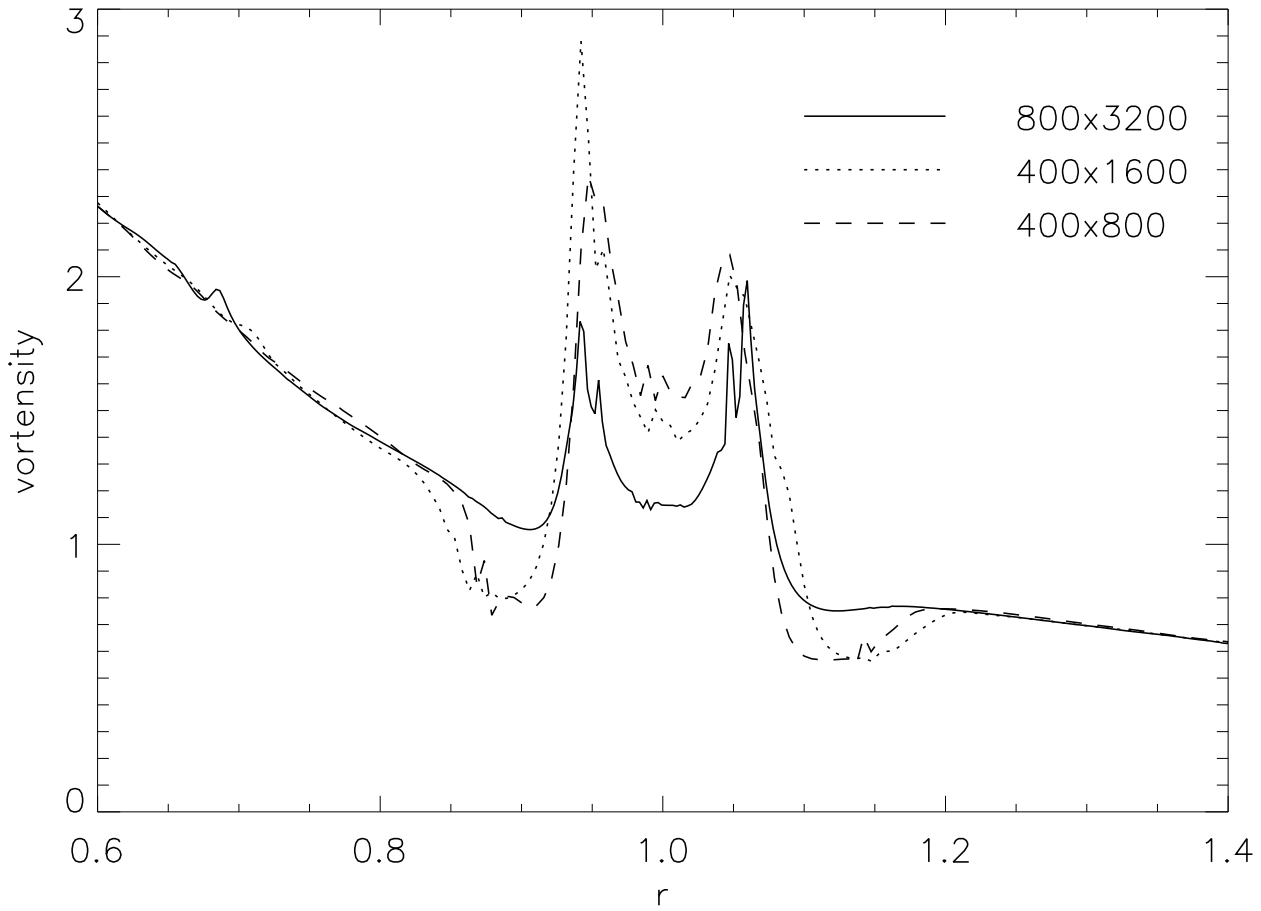


Fig. 8.— Vortensity profiles around the coorbital regions for runs with different resolutions at  $t \approx 70$  orbits. All of them show maxima within the coorbital region.

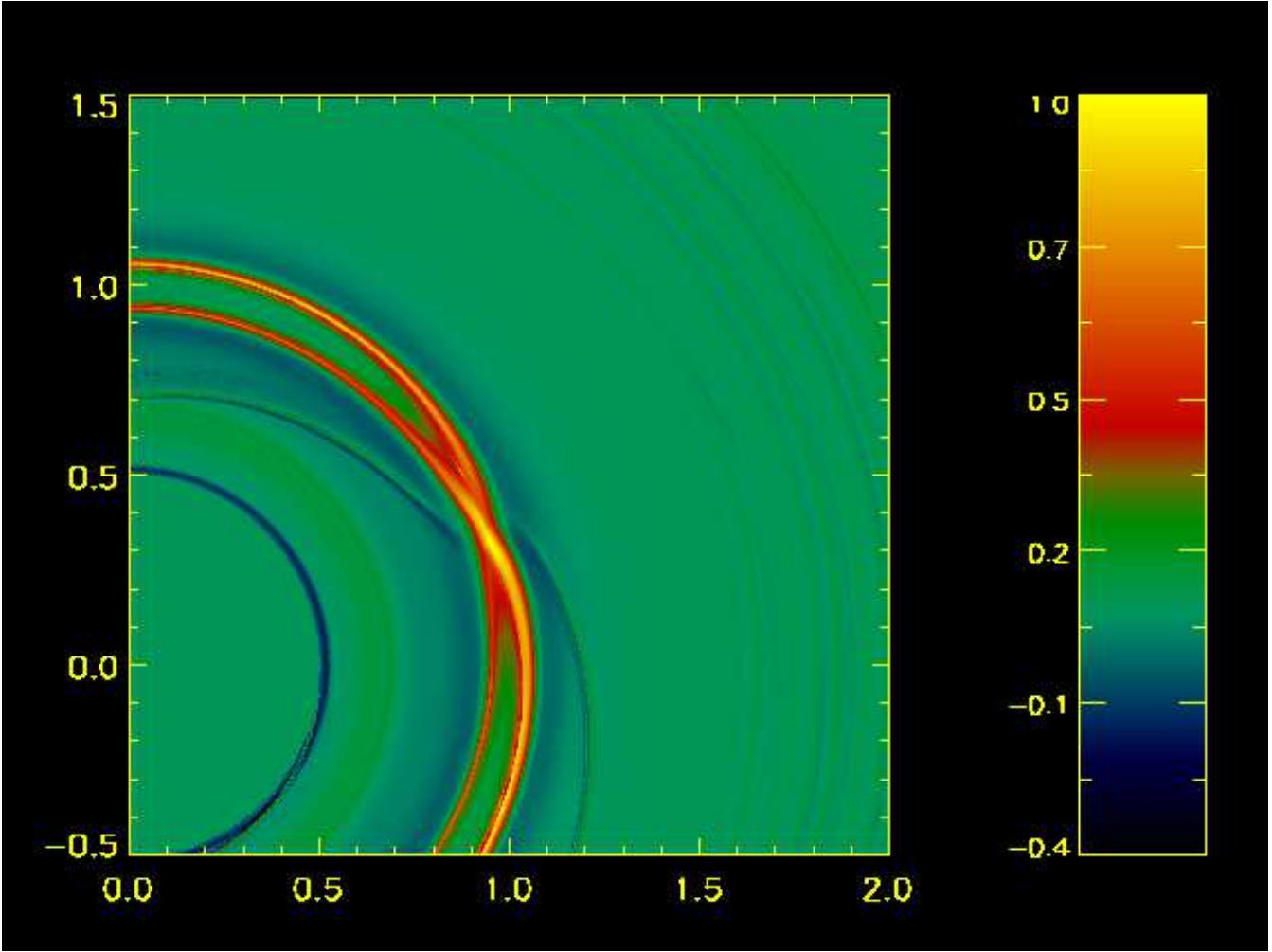


Fig. 9.— Distribution of vortensity increment around the planet at  $t \approx 70$  orbits for the run with resolution  $800 \times 3200$ . (The initial background vortensity is subtracted.) Shocks are well resolved. Vortensity is generated within the coorbital region, especially in the Roche lobe, where no shock exists. The azimuthal density gradient within the same region acts as a source term of vortensity generation (see Figure 10). Note that the vortensity increment within the Roche-lobe is always positive, which contradicts our expectation. We suspect this may be resulted from vortensity mixture in this region.

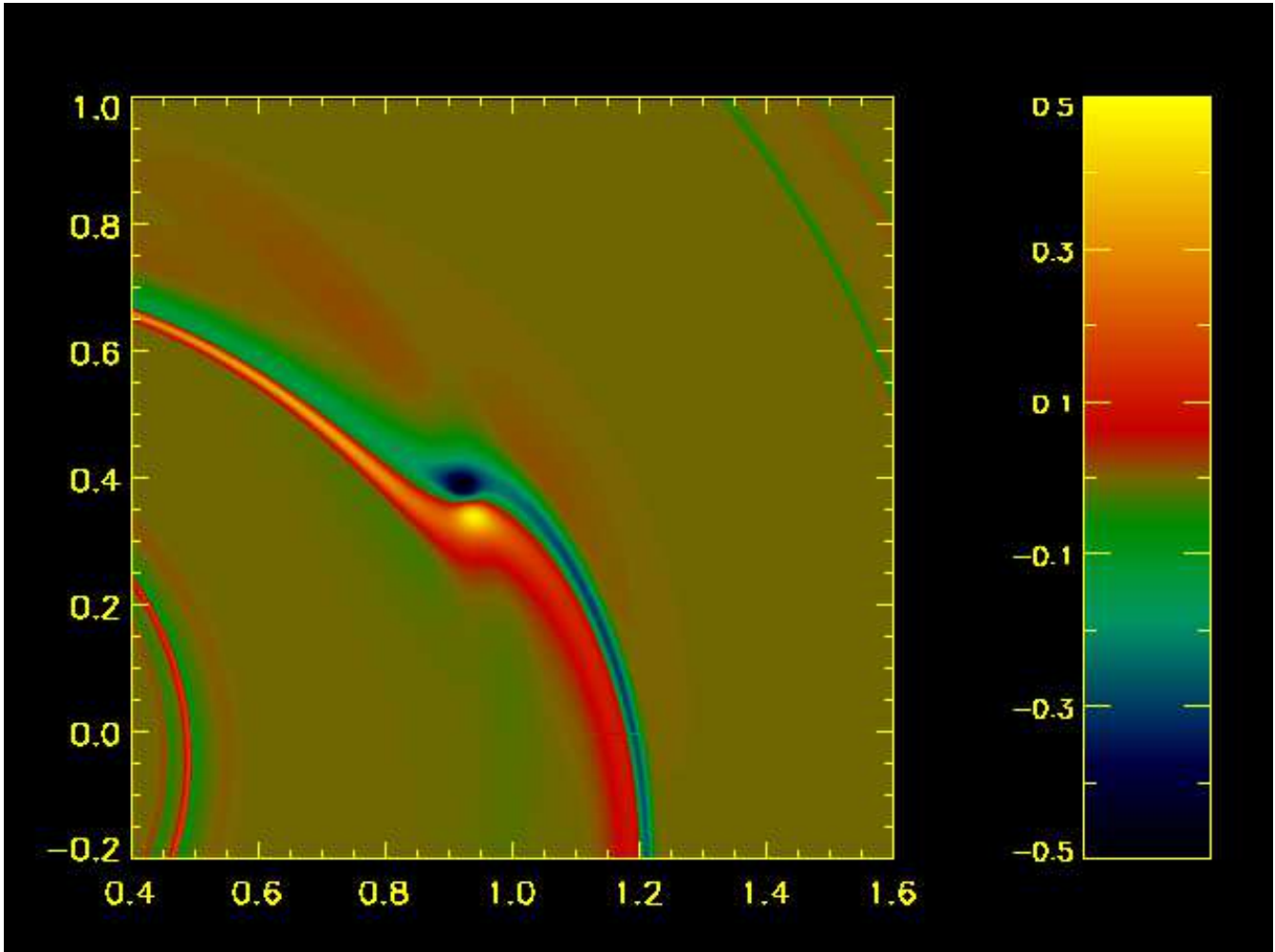


Fig. 10.— Distribution of azimuthal density gradient at the same time as that of Figure 9. Strong density gradient is observed within the Roche lobe and coorbital region.

negative value with smaller oscillations that have a different period from that of earlier oscillations.

We carefully analyzed the evolution between  $t = 80 \sim 120$  orbits and found that the sudden change of the torque’s magnitude is due to the development of a relatively large density blob between the planet and the edge of inner disk as a result of RWIs. During this time, the density blob accumulates materials and augments very quickly because the planet is penetrating the high density region near  $r \sim 0.88$  (which is introduced by the planet’s potential during the first 50 orbits, see the density profile at  $t = 50$  orbits). Consequently, the density blob exerts a stronger torque onto the planet causing the oscillation amplitude of the total torque to increase, the averaged torque also becomes increasingly negative during  $t = 80 \sim 100$  orbits. After the planet passed the high density region at  $t \approx 100$  orbits, the large density blob saturates and wanes; the torque gradually returns back to a value close to zero. However, smaller density blobs do survive and contribute to smaller oscillations of the total torque in the late evolution. Figure 13 shows the density colormaps of the disk at  $t \approx 100$  orbits when the planet is penetrating the high density region, a pronounced density blob (green arc-like structure) in the edge of the inner disk is clearly visible. For comparison, similar plot for  $t \approx 200$  orbits is shown in Figure 14, where previous large density blob diminishes and only small density blob survives both in the inner disk and outer disk. In order to have a better view of the time behavior of the density azimuthal asymmetry between the planet and the outer edge of the inner disk, the radially-averaged density azimuthal distributions of this ring-belt at different times are plotted in Figure 15. Besides some sharp spikes that signal the locations of the planet, density azimuthal asymmetry with different degrees is clearly seen. We note that the density blob has the highest value at  $t \approx 104$  orbits, which coincides with the time when the torque has the negative maximum value and when the planet is penetrating the high density region at  $r \approx 0.88$ . This further supports our analysis on the correlation between the torque magnitude and the augmentation of the density blob.

As a consequence of this interesting phenomenon, the planet’s radius decays quickly during  $t = 80 \sim 120$  orbits, but the decaying slows down after  $t \approx 110$  orbits (see bottom panel of Figure 12 for this non-monotonic behavior). We measured the migration timescale  $\tau_{mig}$ , which is defined as the time needed for the planet to migrate from  $r = 1$  to the central star given a drifting speed measured at the end of our simulation. Our measurement yields  $\tau_{mig} \approx 1300$  orbits, which is almost an order of magnitude lower than that of type II migration from a similar study (Nelson et al. 2000, see their Table 1. Note that their planet also locates at  $r = 1$  initially.). This timescale is consistent with type I migration timescale, which ought to be one or two orders of magnitude lower than that of type II (Ward 1997).

We note that there is a trend for the averaged torque to approach zero at late times, this is probably because the mass of the disk interacting with the planet decreases as it moves in. On the other hand, the oscillation amplitude of the torque induced by RWIs remains relatively constant, it is possible that as the planet moves closer to the host star a turning point may eventually appear, where the RWI-induced torque beats over the Lindblad torque. If this is true, the planet may be halted at certain radial range. Since the planet is very close to the inner edge of our computational

grid at the end of this simulation, we decided to stop the simulation and will address these issue in future investigations.

In the limited time evolutions of a freely moving planet presented here, RWIs do not change the overall picture of inward migration; but they have significant influence on the torque exerted on the planet and consequently make the migration speed of the planet non-monotonic. Further investigations are needed to study the influence of other factor that may potentially bring in significant changes, such as the “releasing time” of the planet, self gravity of the disk fluid, etc. One important issue is how to properly evaluate the torque from materials near the planet, which is embedded in the disk. In this paper, we computed this bruteforcely in 2D. However, many previous studies (Masset 2002; D’Angelo et al. 2005; Li et al. 2005) used quasi-3D treatment, which tends to reduce the torque. It is very likely that if proper 3D treatment is adopted, the total torque will be reduced and the influence of RWIs will be much stronger. This could potentially cause the migration to be reversed.

## 5. Conclusion and Discussion

We have carried out high resolution simulations on the interaction between a protoplanetary disk and an embedded planet with emphasis on detailed interplay between a disk and a planet under the influence of baroclinic generation of vortensity and non-axisymmetric RWIs. Our results are consistent with classical analysis on the interaction between a protoplanetary disk and an embedded planet through Lindblad torques. We confirmed previous studies by Koller et al. (2003) and Li et al. (2005) that non-axisymmetric RWI is likely to develop under certain circumstances and have an important influence on the migration of a planet inside an inviscid disk. We also found that the generation of vortensity (PV) is more common and effective in disks with non-barotropic EOS through the baroclinic instability, which further favors the development of RWIs. As the asymmetry of the density distribution induced by RWIs becomes prominent, the resulting density blobs exert periodical and enhanced gravitational pull onto the planet as they pass by the vicinity of the planet, which causes the total torque received by the planet undergo large amplitude oscillations. Although in our current simulations, RWIs did not change the overall picture of an inward migration, they definitely have very important and interesting effect on the migration speed. As a side effect of an inwardly migrating planet, RWIs introduce nonaxisymmetric density blobs along the way. These enhanced density blobs with strong vortices may help rapid formation of new planet cores within them in a way suggested in (Klahr & Bodenheimer 2006; Petersen et al. 2006), especially in inner regions of circumstellar disks where rapid precipitation and coagulation of solid materials are likely to happen (Silverstone et al. 2006). If these new-born cores could survive during the migration of a giant planet (Chambers 2006; Raymond et al. 2006), they may produce Earth-like planets in the Habitable Zones (Ji et al. 2006) or Hot Earths interior to a close-in giant planet (Raymond et al. 2006).

The study presented here is just a very limited step among many efforts toward understanding

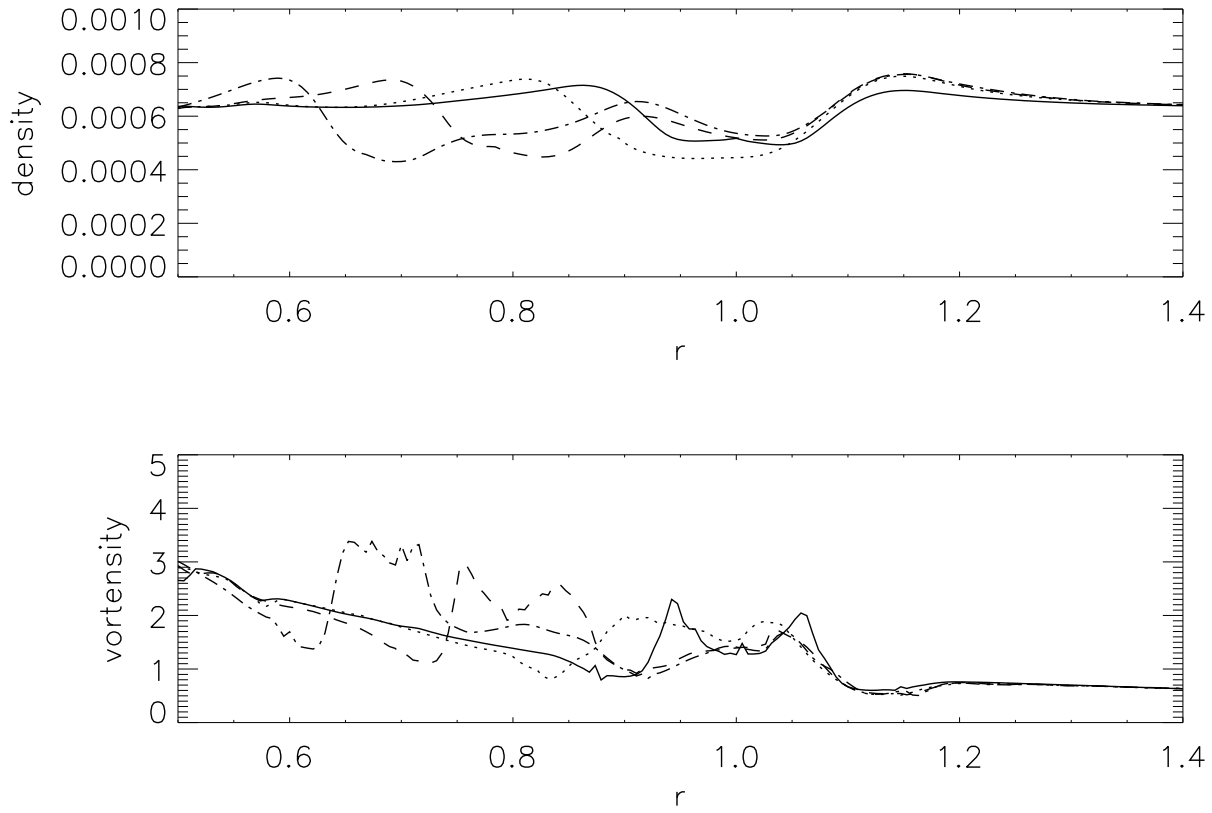


Fig. 11.— The same as Fig. 4 but for a run at  $t \approx 50$  (solid line), 100 (dotted line), 150 (dashed line), and 200 (dash-dotted line) orbits, in which a Neptune mass planet is allowed to move after 50 orbits.

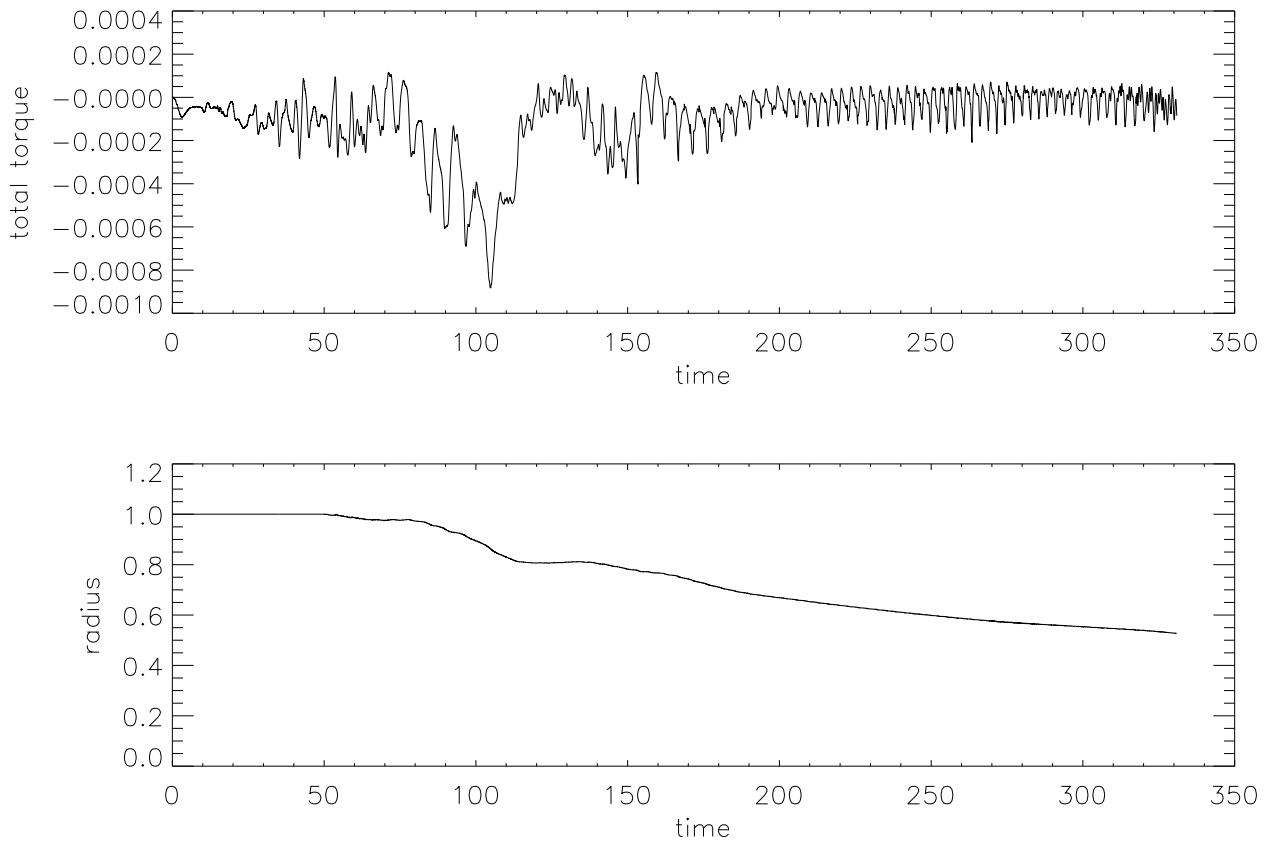


Fig. 12.— Time evolutions of the total torque (top) exerted on a Neptune mass planet by the disk and the radius of the planet (bottom) for the run in which the planet is allowed to move. Raw data is shown. A non-monotonic behavior for the migration speed is observed.



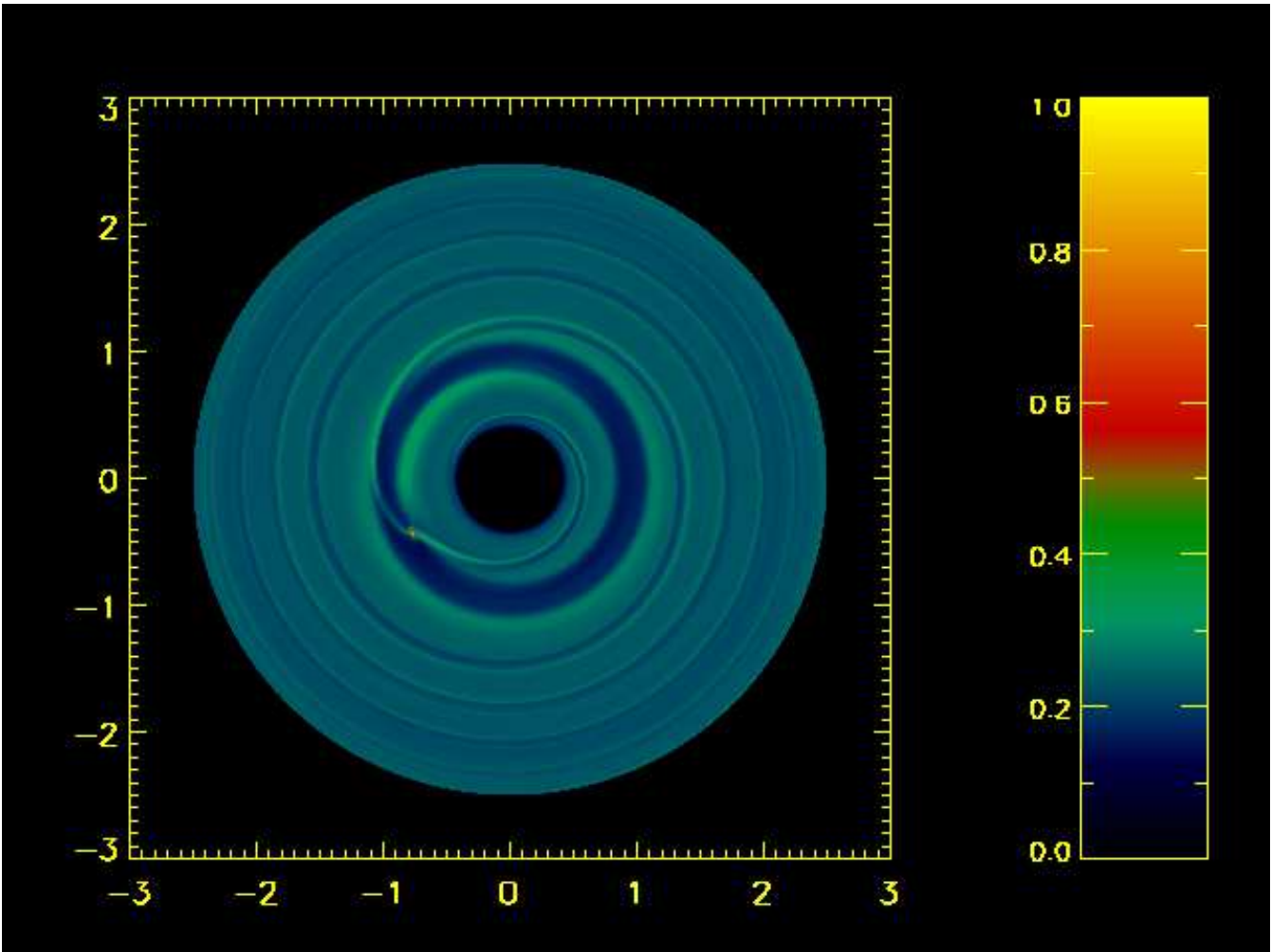


Fig. 13.— The same as Fig. 5 but at  $t = 103$  orbits for a run, in which a Neptune mass planet is allowed to move. The planet is penetrating the high density region around  $r \sim 0.88$  and a fairly large density blob forms (green arc-like structure at the edge of inner disk).

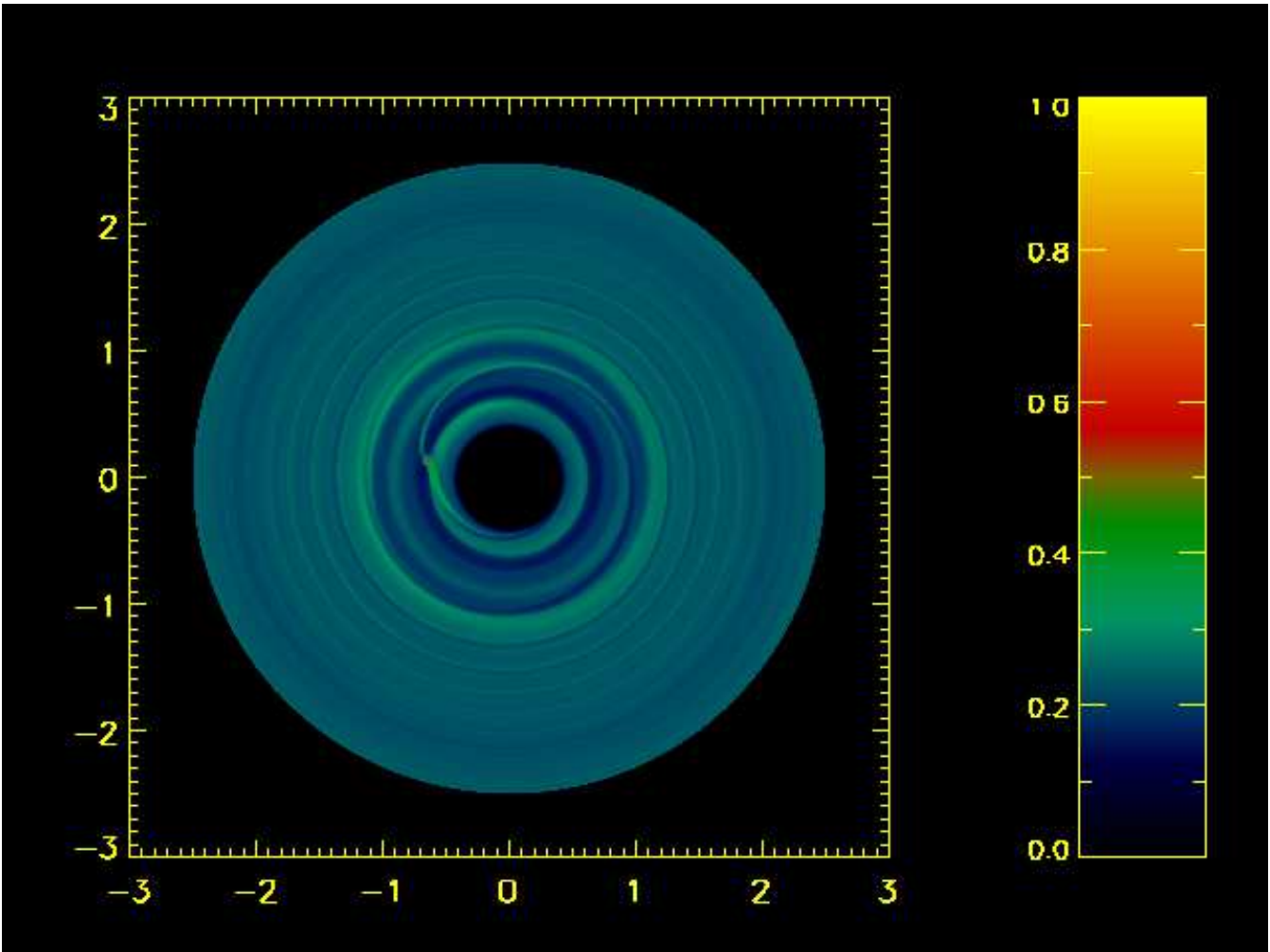


Fig. 14.— The same as Fig. 13 but at  $t = 202$  orbits. The planet has passed the original high density region around  $r \sim 0.88$ . Previous large density blob wanes, smaller density blobs survive at several locations.

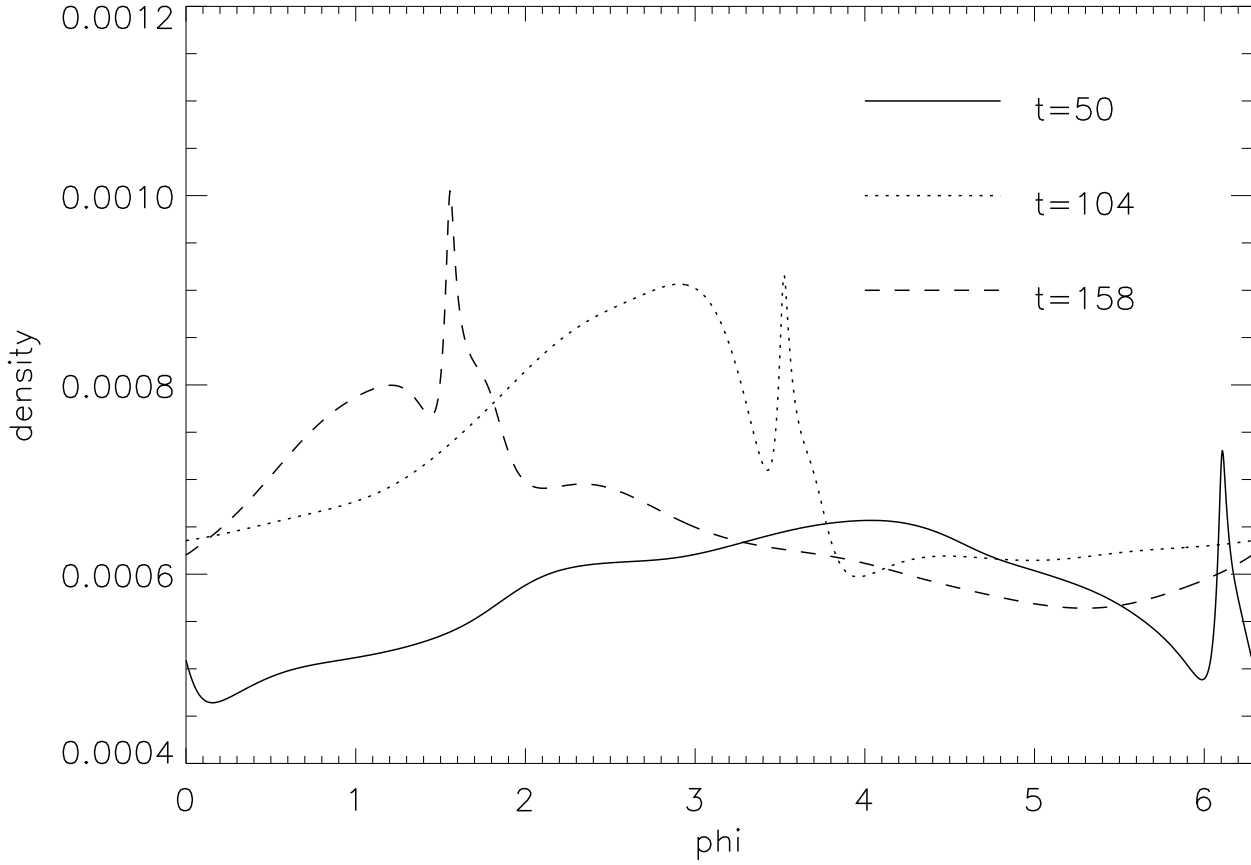


Fig. 15.— The radially-averaged azimuthal density distribution of the ring belt between the planet and the outer edge of the inner disk from a run in which a neptune mass planet is allowed to move. Note that the density blob has the highest value at  $\phi \approx 3$  and  $t \approx 104$  when the planet is penetrating the high density region around  $r \approx 0.88$ . (The spikes reveal the locations of the planet.)

disk-planet interactions. Compared to realistic situations, there are so many physics missing in our much-simplified simulations, the influence of RWIs on planet migration is still not clear in cases where all the physics are correctly taken into account. For example, if the self-gravity of the disk ignored in this study is included in the dynamics of the fluid, it is likely to enhance the RWIs because the gravitational potential field is made more asymmetric by the non-axisymmetric density distribution and more masses will be trapped into potential wells of these density blobs. Enhanced RWIs will exert a stronger positive torque onto the planet and may greatly reduce the migration speed. On the other hand, because RWI develops mostly around the coorbital region where corotation torques are originated, it may have important effect on type III migration. These issues need to be addressed in future investigations.

We thank Hui Li for useful discussions and suggestions during the course of this study. We also thank Joel Tohline for helpful comments and kind permission to use LSU astrophysical hydrodynamics code. We appreciate an anonymous referee for suggesting various ways to analyze our results. S.O. was partially supported by NSF grant AST-0407070 and Center for Computation and Technology at Louisiana State University. J.H.J. is much grateful to Paul Butler for the hospitality during the visit stay at DTM and also appreciates the astronomy group therein. J.H.J. acknowledges the financial support by the National Natural Science Foundations of China (Grants 10573040, 10673006, 10203005, 10233020) and the Foundation of Minor Planets of Purple Mountain Observatory. The computations were performed on the Supermike cluster, the Pelican cluster, the Nemeaux cluster at LSU, and IBM P5 clusters of Louisiana Optical Network Initiative.

## REFERENCES

- Bate, M.R., Lubow, S.H., Ogilvie, G.I., Miller, K.A., 2003, MNRAS, 341, 213
- Butler, R. P., et al. 2006, ApJ, 646, 505
- Chambers, J.E., 2006, ApJ, 652, in press, astro-ph/0610905
- D’Angelo, G., Bate, M.R., Lubow, S. H., 2005, MNRAS, 358,316
- Ford, E. B., Rasio, F. A., & Sills, A. 1999, ApJ, 514, 411
- Goldreich, P., Tremaine, S., 1978, ApJ, 222, 850
- Ida, S., & Lin, D.N.C. 2004, ApJ, 604, 388
- Ji, J. H., Kinoshita, H., Liu, L., & Li, G.Y., 2007, ApJ, 657, 1092
- Klahr, H.H., Bodenheimer, P., 2003, ApJ, 582, 869
- Klahr, H.H., Bodenheimer, P., 2006, ApJ, 639, 432

- Kley, W. 1999, MNRAS, 303, 696
- Kley, W., D’Angelo, G., Henning, T., 2001, ApJ, 547, 457
- Koller, J., Li, H., Lin, D.N.C., 2003, ApJ, 596, 91
- Li, H., Finn, J. M., Lovelace, R. V. E., & Colgate, S. A., 2000, ApJ, 533, 1023
- Li, H., Colgate, S. A., Wendroff, B., Liska, R., 2001, ApJ, 551, 874
- Li, H., Li, S., Koller, J., Wendroff, B. B., Liska, R. Orban, C. M., Liang, E. P.T., Lin, D. N.C., 2005, ApJ, 624, 1003
- Lin, D.N.C., Papaloizou, J.C.B., 1980, MNRAS, 191, 37
- Lin, D.N.C., Papaloizou, J.C.B., 1986, ApJ, 309,846
- Lin, D. N. C., Bodenheimer, P., & Richardson, D. C. 1996, Nature, 380, 606
- Lissauer, J.J. 1993, ARA&A, 31, 129
- Lovelace, R. V. E., Hohlfield, R. G., 1978, ApJ, 221, 51
- Lovelace, R. V. E., Li, H., Colgate, S. A., Nelson, A. F., 1999, ApJ, 513, 805
- Masset, F.S., 2001, ApJ, 558, 453
- Masset, F.S., 2002, A&A, 387, 605
- Masset, F.S., Papaloizou, J.C.B., 2003, ApJ, 588, 494
- Mayor, M., & Queloz, D. 1995, Nature, 378, 355
- Motl, P. M., Tohline, J. E., & Frank, J. 2002, ApJS, 138, 121
- Murray, M., Hansen, B., Holman, M., Tremaine, S., 1998, Science, 279, 69
- Nelson, R.P., Papaloizou, J.C.B., Masset, F., Kley, W., 2000, MNRAS, 318, 18
- Nelson, A., Willy, B., 2003, ApJ, 589, 543
- Ou, S., Tohline, J.E., 2006, ApJ, 651, 1068
- Papaloizou, J. C. B., Nelson, R. P., Masset, F., 2001, A&A, 366, 263
- Petersen, M.R., Stewart, G.R., Julien, K., astro-ph/0611526
- Pollack, J. B., Hubickyj, O., Bodenheimer, P., Lissauer, J. J., Podolak, M., & Greenzweig, Y. 1996, Icarus, 124, 62

- Rasio, F. A., Ford, E.B., 1996, *Science*, 274, 954
- Raymond, S. N., Mandell, A. M., & Sigurdsson, S. 2006, *Science*, 313, 1413
- Safronov, V.S. 1969, *Evolution of the Protoplanetary Cloud and Formation of the Earth and the Planets* (Moscow:Nauka)
- Silverstone, M.D., et al., 2006, *ApJ*, 639, 1138
- Stone, J.M., Norman, M.L., 1992, *ApJS*, 80, 753
- Tohline, J. E. 1980, *ApJ*, 235, 866
- Trilling, D. E., Benz, W., Guillot, T., Lunine, J.I., Hubbard W.B., Burrows, A., 1998, *ApJ*, 500,428
- de Val-borro, M., Edgar, R. G., Artymowicz, P., Cieliegielag, P., and others, 2006, *MNRAS*, 370, 529
- Ward, W. R. 1997, *Icarus*, 126, 261
- Weidenschilling, S. J., & Marzari, F. 1996, *Nature*, 384, 619
- Williams, H. A., & Tohline, J. E. 1988, *ApJ*, 334, 449